OPEN

NPG Asia Materials (2015) 7, e158; doi:10.1038/am.2014.128

www.nature.com/am

ORIGINAL ARTICLE

Clean synthesis of $Cu_2O@CeO_2$ core@shell nanocubes with highly active interface

Xiao Wang[1], Dapeng Liu[1], Junqi Li[1,2], Jiangman Zhen[1,2] and Hongjie Zhang[1]

The fabrication of multi-component hybrid nanostructures is of vital importance because their two-phase interface could provide a rich environment for redox reactions, which are beneficial for enhancing catalytic performance. Inspired by the above consideration, strongly coupled $Cu_2O@CeO_2$ core@shell nanostructures have been successfully prepared via a non-organic and clean aqueous route without using any organic additive. In this process, an auto-catalytic redox reaction occurred on the two-phase interface, followed by a triggered self-assembly process. Additionally, the size, morphology and composition of the as-obtained nanostructures can be tuned well by varying the reaction temperature, as well as the species and the amount of Cu precursors. The catalytic tests for peroxidase-like activity and CO oxidation have been conducted in detail, and the results confirm a strong synergistic effect at the interface sites between the CeO_2 and Cu_2O components.
NPG Asia Materials (2015) **7,** e158; doi:10.1038/am.2014.128; published online 23 January 2015

INTRODUCTION

Interface chemistry has become a relevant field of study in recent years[1–6] because catalytic reactions constantly take place on the surface of catalysts. Therefore, surface states, such as the packing mode of surface atoms, the exposed facets and surface charges, have an important role in determining the feasibility and duration of the reaction. With rapid advances in chemical science, there are many nanomaterials available with well-defined sizes, shapes, crystal facets, structures and compositions.[7–14] There have been increasing efforts to design and control the interface chemistry between different types of components. This is because two-phase interfaces could render hybrid junctions with rich redox reactions, which are beneficial for enhancing the catalytic performance. However, four requirements must be satisfied simultaneously for successful formation of an effective interface: (1) the components should be in full contact; (2) there should be a strong synergistic effect between the two components; (3) to optimize the catalytic properties, the interface areas should be as numerous as possible (a core@shell superstructure seems a good choice); and (4) the richer the redox relationship between the two components is, the better the catalytic properties that they will show. Following the above consideration, the pair formed by the oxidative CeO_2 and the reductive Cu_2O seems ideal, and their hybrid nanostructures are thus desired to obtain highly active interfaces.[15,16]

Unfortunately, few works have been reported on the successful hybridization of CeO_2 and Cu_2O components via the classic two-step process. The main reason for the lack of successful hybridization is that the preformed Cu_2O cores cannot withstand the conditions during the coating of CeO_2 in the following step (Cu_2O could be severely etched by ammonium, which is indispensable during the CeO_2 coating process). However, recently, an important one-step synthetic strategy called 'clean synthesis'[17–23] inspired us to solve this problem. Herein, 'clean' means not only free of toxic raw materials, especially organic compounds, but also low-cost and low-temperature aqueous synthesis, a surface free of residues and a greatly simplified post-treatment process, which are extremely valuable for practical applications. In this strategy, $Ce(OH)_3$ and unsaturated oxides, such as $WO_{2.72}$, are the most reported reductant precursors due to their strong reducing capability, whereas noble metal ions, such as $Ag(NH_3)_2^+$ and $PtCl_4^{2-}$, serve as the oxidant precursors.[18,21–23] These clean synthesis routes are mainly based on the redox principle: an auto-catalytic redox reaction followed by an spontaneous self-assembly process. During the reaction, mutual inhibition between different components generates final products with a uniform structure in the nanometer scale, uniform metal dispersion, tunable metal particle size and narrow metal particle size distribution. Owing to their clean surfaces, the unique nanostructures and their strongly coupled two-phase interface exhibited excellent catalytic activities and high-temperature stabilities compared with those samples prepared with classic two-step processes.

Our group has continuously focused on the fabrication of CeO_2-based, multi-component, hybrid nanostructures.[24–27] Notice that in alkaline solution, $Cu(OH)_2$ has a strong oxidation ability, which has been successfully used as Fehling's solution to detect reducing sugar. In addition, in our previous study, it is found that $Ce(OH)_3$ could serve as a reducer in aqueous solution. In this work, following the above consideration, a two-phase interface reaction has been triggered only in water without the use of any organic components.

[1]State Key Laboratory of Rare Earth Resource Utilization, Changchun Institute of Applied Chemistry, Chinese Academy of Sciences, Changchun, China and [2]Graduate School of the Chinese Academy of Sciences, Beijing, China
Correspondence: Professor D Liu or Professor H Zhang, State Key Laboratory of Rare Earth Resource Utilization, Changchun Institute of Applied Chemistry, Chinese Academy of Sciences, Changchun 130022, China.
E-mail: liudp@ciac.ac.cn or hongjie@ciac.ac.cn
Received 11 July 2014; revised 24 October 2014; accepted 16 November 2014

EXPERIMENTAL PROCEDURE

Synthesis of 155 nm $Cu_2O@CeO_2$ cubes

20 ml of H_2O was bubbled with Ar gas for 5 min to remove O_2. Then, 1 ml of a 0.1 M $Ce(NO_3)_3$ aqueous solution was added, followed by 0.5 ml of 1 M NaOH. Finally, 1 ml of 0.1 M $Cu(NO_3)_2$ was added at 40 °C. The solution was protected by Ar gas. The products were purified by centrifugation at 8000 r.p.m. and then dispersed in 20 ml of water. The size-separation process was carried out by centrifuging at 3500–4000 r.p.m. for 5 min; this was repeated several times to separate the free CeO_2 nanoparticles (NPs) from the solution.

Large-scale synthesis

The large-scale synthesis was similar to the above procedure but with larger volumes (200 times) of the solutions and using the raw material.

Synthesis of CeO_2–Cu_2O branches

First, 20 ml of H_2O was bubbled with Ar for 5 min to remove O_2. Then, 1 ml of 0.1 M $Ce(NO_3)_3$ was added, followed by 0.5 ml of 1 M NaOH. Finally, 0.5 ml of $Cu(NO_3)_2$ was added. The solution was protected by Ar and kept at 40 °C for 1 h.

Control (1)

The synthesis was extremely similar to that of 155 nm CeO_2–Cu_2O cubes except for using 0.7 ml of $Cu(NO_3)_2$ instead of 1 ml of $Cu(NO_3)_2$.

Control (2)

The synthesis was very similar to that of 155 nm CeO_2–Cu_2O cubes except for using 0.7 ml of NaOH instead of 0.5 ml of NaOH.

Synthesis of 68 nm $Cu_2O@CeO_2$ cubes

The synthesis process was similar to that of 155 nm CeO_2–Cu_2O cubes except the temperature was increased to 50 °C.

Synthesis of 44 nm $Cu_2O@CeO_2$ cubes

The synthesis process was similar to that of 155 nm CeO_2–Cu_2O cubes except the temperature was increased to 60 °C.

Synthesis of 32 nm $Cu_2O@CeO_2$ cubes

The synthesis process was similar to that of 155 nm CeO_2–Cu_2O cubes except the temperature was increased to 70 °C.

Characterization

X-ray diffraction (XRD) patterns of the products were collected on a Rigaku-*D*/max 2500 V X-ray diffractometer (Rigaku company, Tokyo, Japan) with Cu-K_α radiation ($\lambda = 1.5418$ Å) and voltage and current of 40 kV and 40 mA, respectively. Transmission electron microscopic (TEM) images were obtained with a TECNAI G2 high-resolution TEM operating at 200 kV. The catalytic performances of the catalysts were monitored on-line using gas chromatography (GC9800).

Catalytic test

CO oxidation. For this reaction, 25 mg of catalyst was placed in a stainless-steel reaction tube. The experiment was performed under the flow of a reactant gas mixture (1% CO, 20% O_2, balance N_2) at a rate of 30 ml min^{-1}.

3,3,5,5-Tetramethylbi-phenyl dihydrochloride oxidation. First, 100 µl of 30% H_2O_2 and 100 µl of 0.01 M 3,3,5,5-Tetramethylbi-phenyl dihydrochloride (freshly prepared) were added to 3 ml of a buffer solution of pH = 5.5. Then,

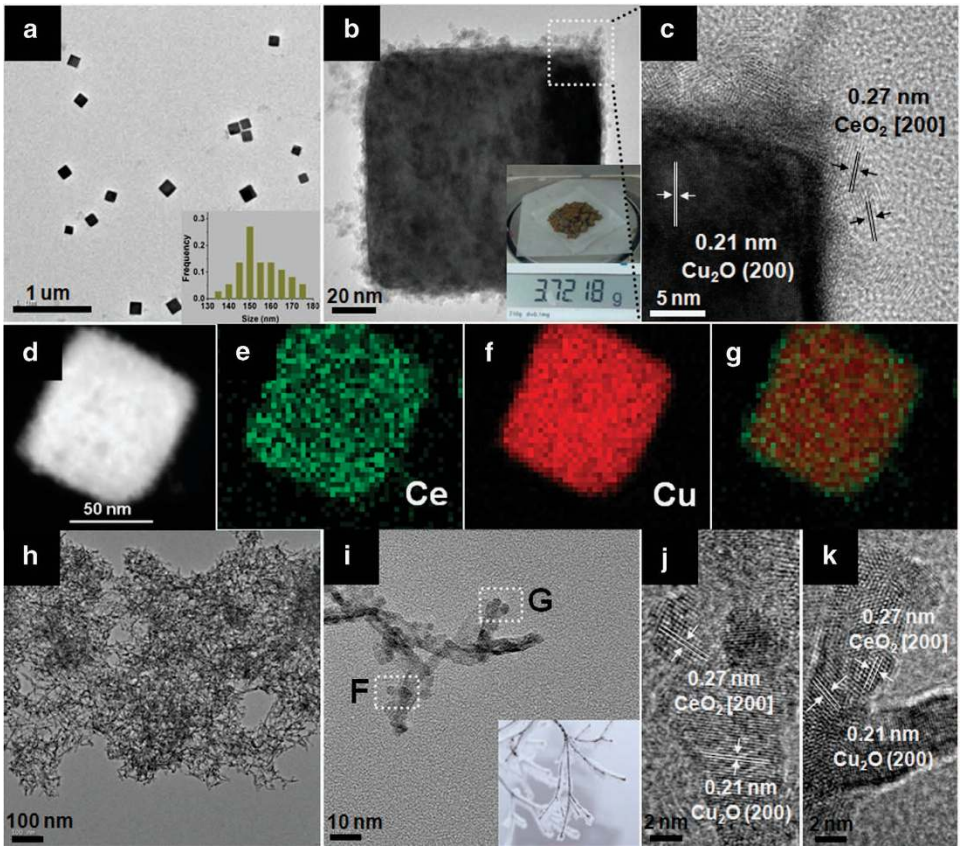

Figure 1 TEM images of $Cu_2O@CeO_2$ cubes (**a**–**c**). The size distribution histogram (**a**, inset); scanning transmission electron microscopy-energy dispersive X-ray spectroscopy analyses of $Cu_2O@CeO_2$ cubes (**d**–**g**); TEM images of Cu_2O–CeO_2 branches (**h**–**k**). The photo (**i**, inset) is of the rime (crust) on branches. All of these TEM images are taken on Mo mesh. TEM, transmission electron microscope.

20 μl of a NP suspension was added to the above mixture. The oxidation reaction progress was monitored at 40 °C.

RESULTS AND DISCUSSION

The XRD analyses of the Cu_2O–CeO_2 hybrid samples are shown in Supplementary Figure 1. The peaks at 2θ = 28.5°, 33.0°, 47.4° and 56.3° can be indexed to the (111), (200), (220) and (311) CeO_2 fluorite-phase reflections (JCPDS No. 34-0394), respectively. The other two strong peaks at 2θ = 36.5° and 42.4° correspond to the pure (111) and (200) Cu_2O reflections (JCPDS No. 65-3288), respectively. There is an obvious broadening in the diffraction peaks of CeO_2, indicating a small particle size in both samples. The particle size of CeO_2, estimated using the Scherrer equation and the XRD patterns, is ~5 nm, which is in agreement with the TEM analysis. The compositions of CeO_2 and Cu_2O in the Cu_2O–CeO_2 hybrid samples and their corresponding UV-Vis absorption spectra have been shown in Supplementary Table 1 and Figure 2, respectively.

TEM images show that the as-obtained Cu_2O–CeO_2 hybrids are sub-155-nm (Figure 1a) uniform core@shell cubes with a rough surface (Figure 1b) when 1.0 ml of the 0.1 M $Cu(NO_3)_2$ aqueous solution (molar ratio of $Cu/Ce/OH^- = 1/1/5$) was added (see the Experimental procedure section for details). A thin CeO_2 layer can be observed clearly on each Cu_2O cube core. The layer is composed of hundreds of self-assembled, 5-nm CeO_2 NPs, which could be easily distinguished in the high-resolution transmission electron microscopy image (Figure 1c). The lattice spacing of 0.27 nm corresponds well to the characteristic (200) planes of the fluorite phase of CeO_2, and the 0.21 nm lattice spacing corresponds to the characteristic (200) planes of the Cu_2O cubic phase, in agreement with XRD results. Further scanning transmission electron microscopy-energy dispersive X-ray spectroscopy analyses have also been done in order to confirm that nature of the core@shell hybrid nanostructure. With the data shown in Figures 1d–g, Cu is present only in the core position, and Ce is distributed everywhere. Here, it should be noticed that our clean and fast method can easily achieve mass production because 3.7218 g of the $Cu_2O@CeO_2$ core@shell cubes can be obtained in one pot (Figure 1b, inset). Brunauer–Emmett–Teller analysis was performed, and the data are shown in Supplementary Figure 7. The Brunauer–Emmett–Teller surface area of Cu_2O–CeO_2 hybrid branches is 151.7 $m^2 g^{-1}$, which is greater than those for $Cu_2O@CeO_2$ cubes (104.2 $m^2 g^{-1}$), commercial Cu_2O (99.2 $m^2 g^{-1}$) and CeO_2 (89.9 $m^2 g^{-1}$) NPs.

The observed color changes give an indication of the whole reaction process. After the $Cu(NO_3)_2$ aqueous solution was injected, the solution immediately became blue, a characteristic color for Cu $(OH)_2$. The redox reaction between $Ce(OH)_3$ and Cu precursors did not occur until the reaction was heated to 40 °C. The reaction was evident by the slow color change to yellow, a typical color for Cu_2O. Obviously, the reaction underwent two steps: the nucleation of the Cu precursor at the beginning, followed by the redox reaction between the $Ce(OH)_3$ and Cu precursors.

Table 1 Summary of the synthetic conditions of CeO_2–Cu_2O hybrids with different nanostructures

	R^a	$T(°C)^b$	*Size (nm)*	
			Cu_2O–CeO_2	*CeO_2*
Control (1)	0.7/1/5	40	—	5
Control (2)	1/1/7	40	—	5
Branches	0.5/1/5	40	7 in width	5
Cubes	1/1/5	40	155	5
		50	68	5
		60	44	5
		70	32	5

[a]Molar ratio of $Cu/Ce/OH^-$.
[b]Reaction temperature.

The amount of added Cu^{2+} ions was found to have a strong influence on the final hybrid structures. As shown in Table 1, when only 0.7 ml of the $Cu(NO_3)_2$ (0.1 M) aqueous solution ($Cu/Ce/OH^- = 0.7/1/5$) was added, the uniform cube-like structure disappeared, and the obtained products were thus disordered (Control (1), Supplementary Figure 5). However, a new type of branch-like structure appeared, instead of the cubes and the disordered products, when we further reduced the amount of $Cu(NO_3)_2$ to 0.5 ml ($Cu/Ce/OH^- = 0.5/1/5$); similar 5 nm CeO_2 NPs stick to the Cu_2O components, as shown in Figures 1h and i. In Figures 1j and k, these two components can be distinguished clearly in the branches. The lattice spacings of 0.27 and 0.21 nm correspond well to the characteristic (200) CeO_2 planes and (200) Cu_2O planes, respectively; these peaks are also observed in cubes. To further confirm these two components, an etching experiment with HCl was performed. As a result, the Cu_2O component was removed in both cubes and branches under ambient conditions, and only the 5 nm CeO_2 NPs were observed in the final products (Supplementary Figures 3 and 4).

The amount of NaOH added also significantly influenced the hybrid structure. In the Control (2) experiment, increasing the amount of NaOH ($Cu/Ce/OH^- = 1/1/7$) produced neither cubes nor branches (Supplementary Figure 6). Notice that copper hydroxide has been identified as amphoteric; therefore, it could be redissolved by reacting with excess OH^- to form $Cu(OH)_4^{2-}$:

$$Cu^{2+} + 2OH^- = Cu(OH)_2\downarrow$$

$$Cu(OH)_2 + 2OH^- = Cu(OH)_4^{2-}$$

Furthermore, successful synthesis of $Cu_2O@CeO_2$ cubes requires the $Cu/Ce/OH^-$ ratio to be kept at 1/1/5, where the $Cu(OH)_2$ precipitation acts as the Cu precursor. In the case of Cu_2O–CeO_2 branches, the $Cu/Ce/OH^-$ ratio equals 0.5/1/5 and $Cu(OH)_4^{2-}$ acts as the Cu precursor. This indicates that the different species of Cu precursors should be responsible for the formation of different hybrid structures. The schematic structural formation of Cu_2O–CeO_2 hybrids is depicted in Scheme 1.

After careful consideration, the conclusion was reached that nucleation of the precursor and the redox process might occur simultaneously only when the reaction temperature is higher than 40 °C. Consequently, a series of control experiments were performed by changing the reaction temperature with a constant ratio of $Cu/Ce/OH^-$ at 1/1/5. The synthetic conditions are summarized in Table 1. As shown in Figures 2a–d, when injecting $Cu(NO_3)_2$ at 50 °C, a similar cube-like structure was obtained, but the cube size dramatically decreased to ~68 nm on average; increasing the injection temperature to 60 and 70 °C led to the formation of smaller sub-44 and -32-nm cubes, respectively. With the decrease in size of the hybrid particle, more branched structures were observed. Meanwhile, the corners of the cubes became smoother as the reaction proceeds. However, the dimension of CeO_2 NPs remained unchanged with different sized cubes. The dependence of the size distribution histogram with reaction temperature is shown in Figure 2l, and the whole kinetics-controlled process is depicted in Figure 2m. The changes in the cube size can be explained in the following way. If the nucleation and redox process occur at nearly the same time, Cu_2O cubes are well coated by CeO_2

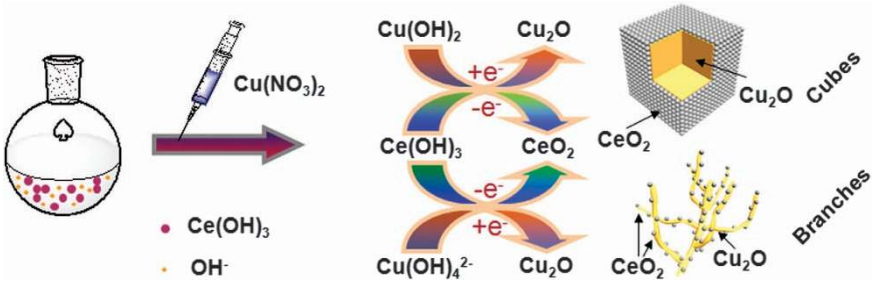

Scheme 1 The preparation process of Cu_2O–CeO_2 hybrids with different Cu/OH^- molar ratios at 40 °C.

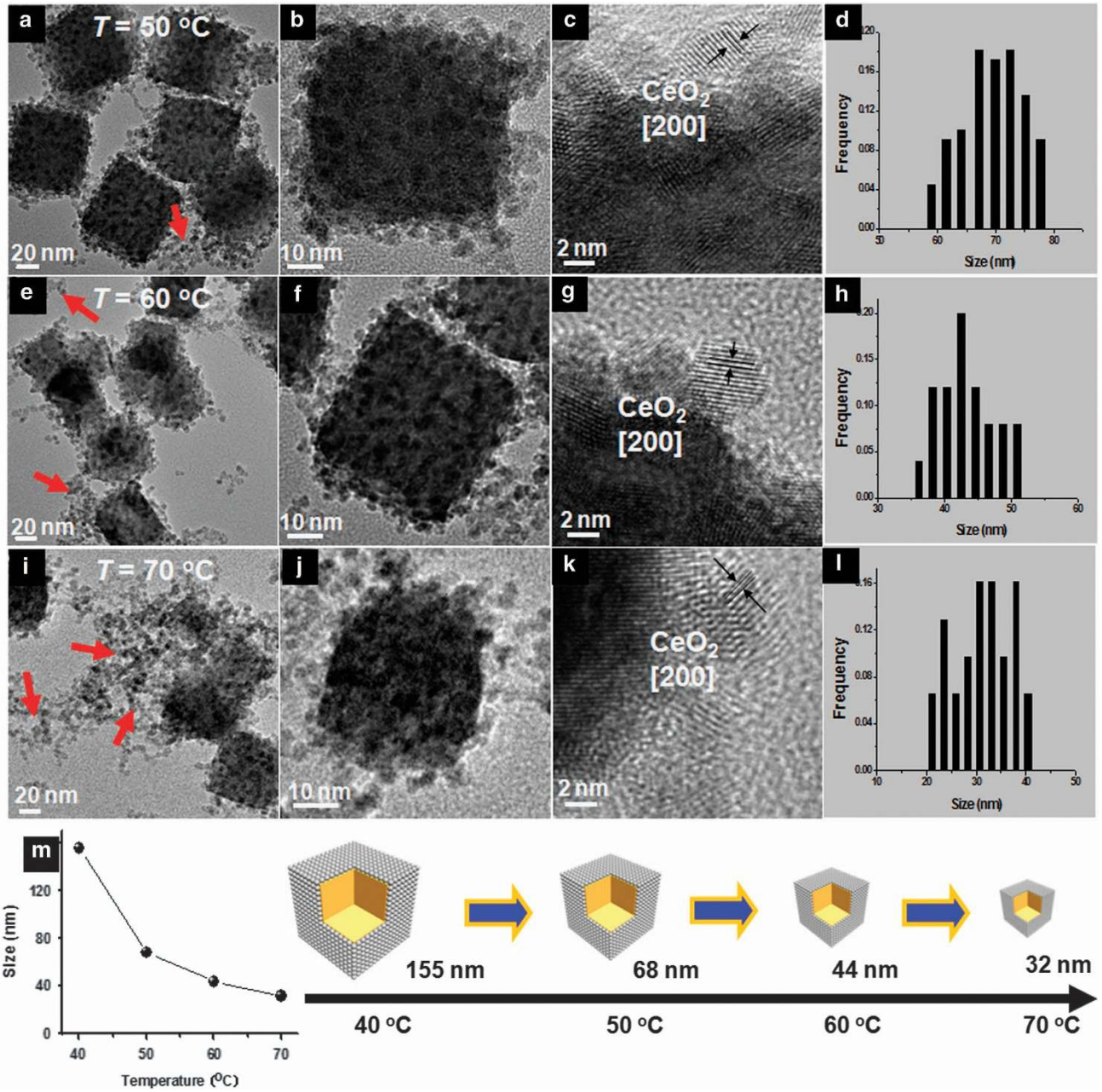

Figure 2 TEM images of $Cu_2O@CeO_2$ cubes obtained via the kinetics-controlled process. Injection of $Cu(NO_3)_2$ at 50 °C (**a**–**d**), 60 °C (**e**–**h**) and 70 °C (**i**–**l**); the relationship between injection temperature and particle size (**m**). From the TEM images, it is easy to see that at higher temperatures, more and more branched structures of CeO_2 on Cu_2O cores are observed and the corners of the cubes become smoother. TEM, transmission electron microscope.

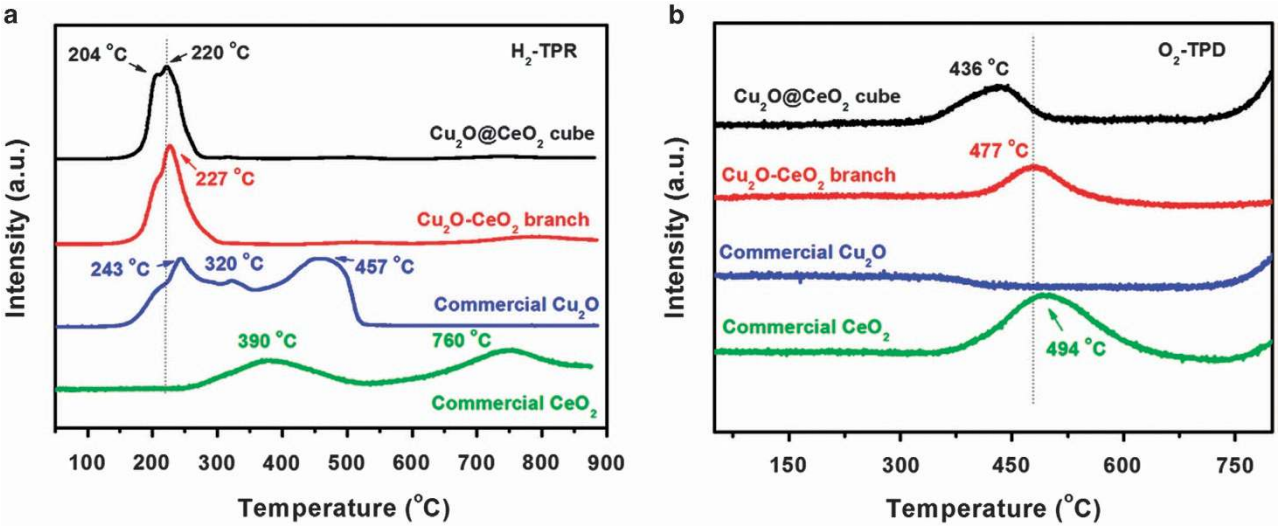

Figure 3 H_2-TPR (**a**) and O_2-TPD (**b**) profiles of $Cu_2O@CeO_2$ core@shell cubes, Cu_2O–CeO_2 branches, pure CeO_2 and Cu_2O. a.u., arbitrary unit; H_2-TPR, H_2-temperature programmed reduction; O_2-TPD, O_2-temperature programmed reduction oxidation.

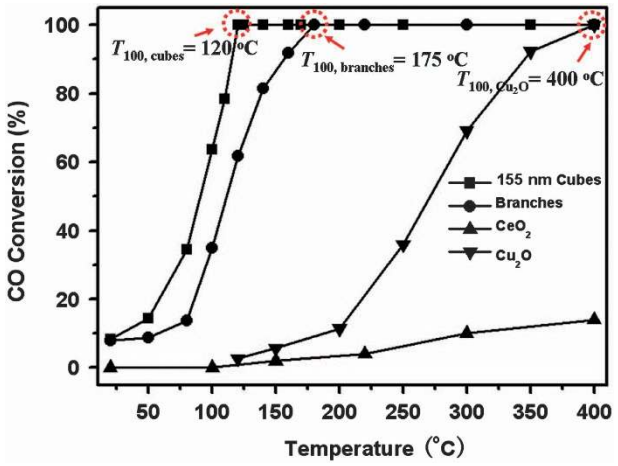

Figure 4 CO conversion curves of $Cu_2O@CeO_2$ cubes (155 nm), Cu_2O–CeO_2 branches, commercial CeO_2 and commercial Cu_2O (T_{100} is the 100% conversion temperature of CO into CO_2).

components right after nucleation and before they continue growing. A higher reaction temperature brings stronger inhibitory effects, which are accompanied by aggregation of naked CeO_2 NPs that increase the CeO_2 coating. That is why the size of Cu_2O cubes and the overall hybrid sizes dramatically decrease. Meanwhile, the strong aggregation tendency of CeO_2 NPs, shown in Figures 2a, e and i (marked by arrows), complicates the separation of the $Cu_2O@CeO_2$ cubes from the reaction system.

In Figure 3a, two broad H_2-temperature programmed reduction peaks observed at 390 and 760 °C for CeO_2 can be attributed to the reduction of surface capping oxygen and bulk oxygen of CeO_2, respectively.[28,29] Comparatively, the commercial Cu_2O sample is highly active, and its first peak appears at ~243 °C. When the two composites, CeO_2 and Cu_2O, are hybridized, the first peak move toward a lower temperature. By careful observation, we found that the temperature of the first reduction peak of the $Cu_2O@CeO_2$ cubes is 204 °C, and the temperature of the first reduction peak of the Cu_2O–CeO_2 branches is 227 °C. The disappearance of the two peaks at 243 and 390 °C has confirmed the existence of synergistic effects between CeO_2 and Cu_2O. Furthermore, O_2-temperature programmed reduction oxidation was used to examine the mobility of the lattice oxygen of oxides. It is seen in Figure 3b that commercial Cu_2O exhibits extremely limited activity and that CeO_2 has a broad peak appearing at 494 °C. According to previous reports, there are two types of oxygen species for oxides: the oxygen adsorbed on the surface and bulk lattice oxygen. The peak at 494 °C should be related to the chemically adsorbed oxygen adjacent to oxygen vacancies.[28] No desorption peak appeared at higher temperatures, indicating that the bulk lattice oxygen is extremely stable in an inert atmosphere. In comparison, the formation of Cu_2O–CeO_2 hybrids decreases the starting temperature of O_2 desorption and the chemically adsorbed oxygen adjacent to the oxygen vacancies. In combination with the H_2-temperature programmed reduction and O_2-temperature programmed reduction oxidation results, Cu_2O could have an important role in activating the oxygen vacancies of CeO_2 so that the two-phase interface becomes an excellent active region for the catalytic reactions.

The catalytic performance of these samples was evaluated first by the model reaction of catalytic CO oxidization. Figure 4 shows the curves of CO conversion as a function of temperature from 20 to 400 °C for samples with $Cu_2O@CeO_2$ cubes (155 nm), Cu_2O–CeO_2 branches, commercial CeO_2 (20–50 nm, Aladdin Company, Shanghai, China) and Cu_2O (Aladdin Company). The temperature T_{100} at which CO is 100% converted follows the sequence: $Cu_2O@CeO_2$ cubes (120 °C) < Cu_2O–CeO_2 branches (175 °C) < commercial CeO_2 (20–50 nm, 400 °C) < commercial Cu_2O (limited activity in the range of testing temperatures). Obviously, $Cu_2O@CeO_2$ cubes present the highest catalytic activity among the samples. Moreover, the activity of $Cu_2O@CeO_2$ cubes is much higher than those of the most typical CuO–CeO_2,[30,31] $Cu_2O@CeO_2$,[15] Pt–CeO_2,[32] and our previously reported Pt@CeO_2[27] and $Co_3O_4@CeO_2$[33] systems. Moreover, at the working temperature of 350 °C, the Ce–Cu cubes and branches remain at 100% yield of CO_2 continuously for up to 10 h (Supplementary Figure 9). We also tested the catalytic performance of the as-obtained $Cu_2O@CeO_2$ cubes at the working temperature of 120 °C. As shown in Supplementary Figure 10, after continuous reaction for 20 h, the sample could convert over 92% CO to CO_2. This indicates that the as-prepared Ce–Cu nanocatalysts have good thermal stability and

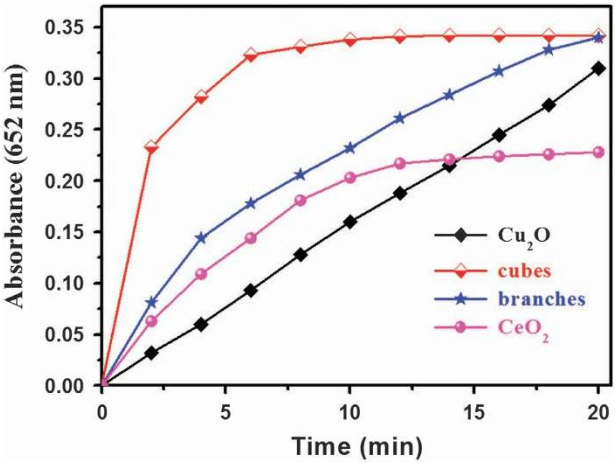

Figure 5 3,3,5,5-Tetramethylbi-phenyl dihydrochloride oxidation curves of Cu_2O@CeO_2 core@shell cubes, Cu_2O–CeO_2 branches, pure CeO_2 and Cu_2O.

excellent catalytic activity, exhibiting the great potential to replace Pt–CeO_2 catalysts.

The peroxidase-like activity of Ce–Cu cubes and branches was evaluated for catalysis of the peroxidase substrate 3,3,5,5-Tetramethylbi-phenyl dihydrochloride in the presence of H_2O_2. In this reaction, we chose a buffer solution with pH = 5.5 and a reaction temperature of 40 °C. The initial oxidation rate is evaluated by monitoring the absorbance increase of the oxidized products of 3,3,5,5-Tetramethylbi-phenyl dihydrochloride at 652 nm (Figure 5). Obviously, the as-obtained Cu_2O@CeO_2 core@shell cubes show a much higher activity than the four given samples during the catalytic oxidation of 3,3,5,5-Tetramethylbi-phenyl dihydrochloride. The Cu_2O–CeO_2 branches also show better catalytic performance than the commercial Cu_2O and CeO_2. The previous reports have shown that the activities of transition metal oxide material-based peroxidase mimics were mostly derived from the metal ions that have a catalytic activity using H_2O_2 as a substrate through a mechanism similar to that of the Fenton reaction.[34,35] Self and co-workers found that cerium ions could also perform a Fenton-like reaction:[35,36]

$$Ce^{3+} + H_2O_2 + H^+ \rightarrow Ce^{4+} + OH^- + H_2O \quad (1)$$

$$OH^- + H_2O_2 \rightarrow HO_2^- + H_2O \quad (2)$$

$$Ce^{4+} + HO_2^- \rightarrow O_2 + Ce^{3+} + H^+ \quad (3)$$

It is obvious that the existence of Ce^{3+} is the key to triggering the reaction. The predictable result is that the higher concentration of Ce^{3+} ions in the reaction solution is, the faster the catalytic reaction should be. For the Cu_2O–CeO_2 hybrid system, the large amount of Cu^+ could react first with H_2O_2 to form HO_2^-. Therefore, before reaction (1) started, the following reaction (4) occurred:

$$Cu^+ + H_2O_2 + H^+ \rightarrow Cu^{2+} + OH^- + H_2O \quad (4)$$

followed by

$$OH^- + H_2O_2 \rightarrow HO_2^- + H_2O \quad (2)$$

$$Ce^{4+} + HO_2^- \rightarrow O_2 + Ce^{3+} + H^+ \quad (3)$$

$$Ce^{3+} + H_2O_2 + H^+ \rightarrow Ce^{4+} + OH^- + H_2O \quad (1)$$

The largely increased amount of Ce^{3+} might be the main reason for the improved, intrinsic, enzyme mimetic activity.

In sum, we have successfully developed a new, non-organic route for the facile, fast and low-cost synthesis of environment-friendly Cu_2O–CeO_2 hybrids with well-controlled nanostructures. Without the addition of any organic reducing agents or surfactants, the whole reaction is a clean redox process between a Cu precursor and $Ce(OH)_3$ in an aqueous solution. The formation of the final hybrid nanostructures depends on the initial species of the Cu precursors. The $Cu(OH)_2$ precursor species yield uniform Cu_2O cubes with a CeO_2 surface coating, whereas $Cu(OH)_4^{2-}$ precursor species lead to asymmetrical Cu_2O–CeO_2 branches. Such an interface engineering strategy favors strong coupling between the two components of CeO_2 and Cu_2O. In the following CO oxidation and peroxidase-like activity tests, the Cu_2O@CeO_2 core@shell cubes exhibited a rather high catalytic activity; we hypothesize that the existence of highly active interfaces is the main reason for this activity. Our new synthetic process opens a new window for better design and preparation of noble metal-free nanocatalysts, which could have great applications in catalysis, gas-sensors and bio-chemistry, as well as areas related to energy and the environment.

Supporting Information

XRD patterns of the as-obtained Cu_2O–CeO_2 branches and cubes; Ultraviolet–visible absorption spectra of Cu_2O–CeO_2 hybrids; TEM images of Cu_2O–CeO_2 cubes and branches after HCl etching; TEM images of the control experiment; and ICP analysis results.

CONFLICT OF INTEREST

The authors declare no conflict of interest.

ACKNOWLEDGEMENTS

This work was supported by financial aid from the National Natural Science Foundation of China (Grant Nos. 91122030, 51272249, 21401186, 21210001 and 21221061), and the MOST of China (Grant No. 2014CB643802).

1 Cui, C., Yu, J., Li, H., Gao, M., Liang, H. & Yu, S. Remarkable enhancement of electrocatalytic activity by tuning the interface of Pd–Au bimetallic nanoparticle tubes. *ACS Nano* **5**, 4211–4218 (2011).
2 Kim, H. & Henkelman, G. CO Oxidation at the interface of Au nanoclusters and the stepped-CeO_2 (111) surface by the Mars–van Krevelen mechanism. *J. Phys. Chem. Lett.* **4**, 216–221 (2013).
3 Zhang, L., Kim, H. & Henkelman, G. CO oxidation at the Au–Cu interface of bimetallic nanoclusters supported on CeO_2 (111). *J. Phys. Chem. Lett.* **4**, 2943–2947 (2013).
4 Liu, H., Zheng, N., Yang, D., Ke, X., Jaatinen, E., Zhao, J. & Zhu, H. Coherent interfaces between crystals in nanocrystal composites. *ACS Nano* **4**, 6219–6227 (2010).
5 Boldt, K., Schwarz, K., Kirkwood, N., Smith, T. & Mulvaney, P. Electronic structure engineering in ZnSe/CdS type-II nanoparticles by interface alloying. *J. Phys. Chem. C* **118**, 13276–13284 (2014).
6 Nguyen, T., Dinh, C. & Do, T. Tailoring the assembly, interfaces, and porosity of nanostructures toward enhanced catalytic activity. *Chem. Commun.* **51**, 624–635 (2014).
7 Xia, X. H. & Xia, Y. N. Symmetry breaking during seeded growth of nanocrystals. *Nano Lett.* **12**, 6038–6042 (2012).
8 Peng, H. C., Xie, S. F., Park, J. H., Xia, X. H. & Xia, Y. N. Quantitative analysis of the coverage density of Br^- Ions on Pd{100} facets and its role in controlling the shape of Pd nanocrystals. *J. Am. Chem. Soc.* **135**, 3780–3783 (2013).
9 Wang, J. W., Sansoz, F., Huang, J. Y., Liu, Y., Sun, S. H., Zhang, Z. & Mao, S. X. Near-ideal theoretical strength in gold nanowires containing angstrom scale twins. *Nat. Commun.* **4**, 1472 (2012).
10 Zhang, S., Metin, O., Su, D. & Sun, S. H. Monodisperse AgPd alloy nanoparticles and their superior catalysis for the dehydrogenation of formic acid. *Angew. Chem. Int. Ed.* **52**, 3681–3684 (2013).
11 Cai, S. F., Duan, H. H., Rong, H. P., Wang, D. S., Li, L. S., He, W. & Li, Y. D. Highly active and selective catalysis of bimetallic Rh_3Ni_1 nanoparticles in the hydrogenation of nitroarenes. *ACS Catal.* **3**, 608–612 (2013).

12 Liu, Y. X., Wang, D. S., Shi, J. X., Peng, Q. & Li, Y. D. Magnetic tuning of upconversion luminescence in lanthanide-doped bifunctional nanocrystals. *Angew. Chem. Int. Ed.* **52**, 4366–4369 (2013).
13 Zhu, J. X., Yin, Z. Y., Yang, D., Sun, T., Yu, H., Hoster, H. E., Hng, H. H., Zhang, H. & Yan, Q. Y. Hierarchical hollow spheres composed of ultrathin Fe_2O_3 nanosheets for lithium storage and photocatalytic water oxidation. *Energy Environ. Sci.* **6**, 987–993 (2013).
14 Wang, Z. Y., Luan, D. Y., Yin, F., Boey, C. & Lou, X. W. Fast formation of SnO_2 nanoboxes with enhanced lithium storage capability. *J. Am. Chem. Soc.* **133**, 4738–4781 (2011).
15 Bao, H., Zhang, Z., Hua, Q. & Huang, W. Compositions, structures, and catalytic activities of $CeO_2@Cu_2O$ nanocomposites prepared by the template-assisted method. *Langmuir* **30**, 6427–6436 (2014).
16 He, C., Yu, Y., Chen, C., Yue, L., Qiao, N., Shen, Q., Chen, J. & Hao, Z. Facile preparation of 3D ordered mesoporous CuO_x-CeO_2 with notably enhanced efficiency for the low temperature oxidation of heteroatom-containing volatile organic compounds. *RSC Adv.* **3**, 19639–19656 (2013).
17 Chen, X. M., Wu, G. H., Chen, J. M., Chen, X., Xie, Z. X. & Wang, X. R. Synthesis of "clean" and well-dispersive Pd nanoparticles with excellent electrocatalytic property on graphene oxide. *J. Am. Chem. Soc.* **133**, 3693–3695 (2011).
18 Xi, G. C., Ye, J. H., Ma, Q., Su, N., Bai, H. & Wang, C. *In situ* growth of metal particles on 3D urchin-like WO_3 nanostructures. *J. Am. Chem. Soc.* **134**, 6508–6511 (2012).
19 Yin, H., Tang, H. J., Wang, D., Gao, Y. & Tang, Z. Y. Facile synthesis of surfactant-Free Au cluster/graphene hybrids for high-performance oxygen reduction reaction. *ACS Nano* **6**, 8288–8297 (2012).
20 Kim, K. W., Kim, S. M., Choi, S., Kim, J. & Lee, I. S. Electroless Pt deposition on Mn_3O_4 nanoparticles via the galvanic replacement process: electrocatalytic nanocomposite with enhanced performance for oxygen reduction reaction. *ACS Nano* **6**, 5122–5129 (2012).
21 Kayama, T., Yamazaki, K. & Shinjoh, H. Nanostructured Ceria – Silver synthesized in a one-pot redox reaction catalyzes carbon oxidation. *J. Am. Chem. Soc.* **132**, 13154–13155 (2010).
22 Mitsudome, T., Mikami, Y., Matoba, M., Mizugaki, T. & Kaneda, K. Design of a Silver–Cerium dioxide core–shell nanocomposite catalyst for chemoselective reduction reactions. *Angew. Chem. Int. Ed.* **50**, 136–139 (2012).
23 Wang, X., Liu, D. P., Song, S. Y. & Zhang, H. J. $Pt@CeO_2$ multicore@shell self-assembled nanospheres: clean synthesis, structure optimization, and catalytic applications. *J. Am. Chem. Soc.* **135**, 15864–15872 (2013).
24 Wang, X., Li, X. Y., Liu, D. P., Song, S. Y. & Zhang, H. J. Green synthesis of Pt/CeO_2/graphene hybrid nanomaterials with remarkably enhanced electrocatalytic properties. *Chem. Commun.* **48**, 2885–2887 (2012).
25 Wang, X., Liu, D. P., Song, S. Y. & Zhang, H. J. Synthesis of highly active Pt-CeO_2 hybrids with tunable secondary nanostructures for the catalytic hydrolysis of ammonia borane. *Chem. Commun.* **48**, 10207–10209 (2012).
26 Wang, X., Liu, D. P., Song, S. Y., Zeng, L. & Zhang, Y. Water-soluble Au-CeO_2 hybrid nanosheets with high catalytic activity and recyclability. *Dalton Trans.* **41**, 7193 (2012).
27 Wang, X., Liu, D. P., Song, S. Y. & Zhang, H. J. Graphene oxide induced formation of Pt-CeO_2 hybrid nanoflowers with tunable CeO_2 thickness for catalytic hydrolysis of ammonia borane. *Chem. Eur. J.* **19**, 8082–8086 (2013).
28 Zuo, Y., Huang, X., Li, L. & Li, G. An ultra-stable nanosized $Ce_{0.9}Fe_{0.1}O_2$ solid solution with an excellent catalytic performance towards CH_4 oxidation. *J. Mater. Chem. A* **1**, 374–380 (2013).
29 Rocchini, E., Trovarelli, A., Llorca, J., Graham, G. W., Weber, W. H., Maciejewski, M. & Baiker, A. Relationships between structural/morphological modifications and oxygen storage–redox behavior of silica-doped ceria. *J. Catal.* **194**, 461–478 (2000).
30 Jia, A. P., Jiang, S. Y., Lu, J. Q. & Luo, M. F. Study of catalytic activity at the $CuO-CeO_2$ interface for CO oxidation. *J. Phys. Chem. C* **114**, 21605–21610 (2010).
31 Hornes, A., Hungria, A. B., Bera, P., Lopez Camara, A., Fernandez-Garcia, M., Martinez-Arias, A., Barrio, L., Estrella, M., Zhou, G., Fonseca, J. J., Hanson, J. C. & Rodriguez, J. A. Inverse CeO_2/CuO catalyst as an alternative to classical direct configurations for preferential oxidation of CO in hydrogen-rich stream. *J. Am. Chem. Soc.* **132**, 34–35 (2010).
32 Zhou, H. P., Wu, H. S., Shen, J., Yin, A. X., Sun, L. D. & Yan, C. H. Thermally stable Pt/CeO_2 hetero-nanocomposites with high catalytic activity. *J. Am. Chem. Soc.* **132**, 4998–4999 (2010).
33 Zhen, J. M., Wang, X., Liu, D. P., Song, S. Y., Wang, Z., Wang, Y. H., Li, J. Q., Wang, F. & Zhang, H. J. $Co_3O_4@CeO_2$ core@shell cubes: designed synthesis and optimization of catalytic properties. *Chem. Eur. J.* **20**, 4469–4473 (2014).
34 Xu, C. & Qu, X. Cerium oxide nanoparticle: a remarkably versatile rare earth nanomaterial for biological applications. *NPG Asia Mater.* **6**, e90. doi:10.1038/am.2013.88 (2014).
35 Gao, L. Z., Zhuang, J., Nie, L., Zhang, J. B., Zhang, Y., Gu, N., Wang, T. H., Feng, J., Yang, D. L., Perrett, S. & Yan, X. Intrinsic peroxidase-like activity of ferromagnetic nanoparticles. *Nat. Nanotechnol.* **2**, 577–583 (2007).
36 Heckert, E. G., Seal, S. & Self, W. T. Fenton-like reaction catalyzed by the rare earth inner transition metal cerium. *Environ. Sci. Technol.* **42**, 5014–5019 (2008).

Supplementary Information accompanies the paper on the NPG Asia Materials website (http://www.nature.com/am)